Simulated Multispectral Temperature and Atmospheric Composition Retrievals for the JPL GEO-IR Sounder

Vijay Natraj[1], Ming Luo[1], Jean-Francois Blavier[1], Vivienne H. Payne[1], Derek J. Posselt[1], Stanley P. Sander[1], Zhao-Cheng Zeng[2,3], Jessica L. Neu[1], Denis Tremblay[4], Longtao Wu[1], Jacola A. Roman[1], Yen-Hung Wu[1], Leonard I. Dorsky[1]

[1]Jet Propulsion Laboratory, California Institute of Technology, Pasadena, CA 91109, USA

[2]Joint Institute for Regional Earth System Science and Engineering, University of California, Los Angeles, CA 90095, USA

[3]Division of Geological and Planetary Sciences, California Institute of Technology, Pasadena, CA 91125, USA

[4]Global Science Technology, USA

Correspondence to: Vijay Natraj (vijay.natraj@jpl.nasa.gov)

Abstract. Satellite measurements enable quantification of atmospheric temperature, humidity, wind fields, and trace gas vertical profiles. The majority of current instruments operate on polar orbiting satellites and either in the thermal/mid-wave or in the shortwave infrared spectral regions. We present a new multispectral instrument concept for improved measurements from geostationary orbit (GEO) with sensitivity to the boundary layer. The JPL GEO-IR sounder, which is an imaging Fourier Transform Spectrometer, uses a wide spectral range (1–15.4 μm), encompassing both reflected solar and thermal emission bands to improve sensitivity to the lower troposphere and boundary layer. We perform retrieval simulations for both clean and polluted scenarios that also encompass different temperature and humidity profiles. The results illustrate the benefits of combining shortwave and thermal infrared measurements. In particular, the former adds information in the boundary layer, while the latter helps to separate near-surface and mid-tropospheric variability. The performance of the JPL GEO-IR sounder is similar to or better than currently operational instruments. The proposed concept is expected to improve weather forecasting, severe storm tracking and forecasting, and also benefit local and global air quality and climate research.

1 Introduction

The Program of Record (PoR) of current and planned satellite observations, as described in the 2017 US Earth Science Decadal Survey (*NASEM*, 2018), includes a range of spectrally-resolved radiance measurements in the thermal and shortwave infrared (TIR and SWIR) wavelength regions that provide key information on atmospheric temperature (TATM), water vapor (H_2O) and a range of trace gases (see Table 1 for a definition of spectral range designations). The TIR region can be further subdivided into midwave, longwave and very longwave infrared (MIR, LWIR and VLWIR) regions. Profiling of key gases including CO, CH_4, and CO_2 with sensitivity to planetary boundary layer (PBL) abundances was identified as a gap in current capability in the 2017 Decadal Survey, as was the promise of multispectral approaches for addressing this gap. In fact, combining radiances from the (thermal emission dominated) TIR and (solar reflection dominated) SWIR spectral regions has been shown to increase the vertical information content for these gases, providing improved information on near-surface variations relative to retrievals from the thermal alone (e.g., *Christi and Stephens*, 2004; *Worden et al.*, 2010; *Kuai et al.*, 2013; *Worden et al.*, 2015; *Fu et al.*, 2016; *Zhang et al.*, 2018; *Schneider et al.*, 2021). Such retrievals have the potential to extend the utility of satellite products for air quality forecasting, greenhouse gas monitoring and carbon cycle research. In addition, combining TIR and SWIR infrared radiances also offers opportunities for increasing the vertical information of H_2O retrievals in the PBL, another topic highlighted by the Decadal Survey and by the NASA Decadal Survey PBL Incubation Study Team (*Teixeira et al., 2021*). Under clear-sky conditions, the SWIR provides sensitivity to H_2O (e.g., *Noël et al.*, 2005; *Trent et al., 2018; Nelson et al., 2016*), CO (e.g., *Buchwitz et al., 2004; Deeter et al., 2009; Landgraf et al., 2016; Borsdorff et al., 2017; 2018*), CH_4 (e.g., *Buchwitz et al.*, 2005; *Frankenberg et al.*, 2006; *Yokota et al.*, 2009; *Hu et al.*, 2018; *Parker et al.*, 2020) and CO_2 (e.g., *Buchwitz et al.*, 2005; *Yokota et al.*, 2009; *O'Dell et al.*, 2018) throughout the full atmospheric column, providing complementary information to the TIR radiances that are strongly sensitive to the details of the profile of TATM, H_2O and trace gases but have variable sensitivity to the PBL, depending on surface and atmospheric conditions.

Table 2 shows a list of current and planned missions making spectrally-resolved, spaceborne TIR and SWIR measurements. In Low Earth Orbit (LEO), the MOPITT instrument on the Terra platform has been providing a record of TIR+SWIR CO for over two decades (*Buchholz et al.*, 2021). GOSAT and GOSAT-2 provide spectrally-resolved TIR and SWIR radiances on the same platform, with coverage of SWIR CO_2 and CH_4 bands, as well as H_2O absorption (*Trent et al.*, 2018), but not SWIR CO. The TROPOMI instrument on the Sentinel-5P satellite flies in formation with the CrIS instrument on the Suomi-NPP satellite, providing near-coincident observations of TIR and SWIR, presenting opportunities

2

for multispectral retrievals of CO and CH_4. Measurements from geostationary (GEO) orbit can provide contiguous horizontal (~4 km) and temporal (full sounding disk coverage in 1–2 hours) resolution not possible from LEO (e.g., *Schmit et al.*, 2009). The IRS instrument onboard the Meteosat Third Generation Sounder platform will track the four-dimensional structure of TATM and H_2O (*Holmlund et al.*, 2021). The GIIRS instrument on the Fengyun-4 meteorological satellite has similar capabilities (*Yang et al.*, 2017). *Adkins et al.* (2021) describe in comprehensive detail the value of a hyperspectral IR sounder in GEO orbit. Based on this report, an advanced high-resolution IR sounder has been recommended for the Geostationary Extended Observations (GeoXO) mission (https://www.nesdis.noaa.gov/next-generation-satellites/geostationary-extended-observations-geoxo). However, none of the current/planned instruments/missions listed in Table 2 provide TIR + SWIR measurements from GEO on the same platform.

Here, we describe an instrument concept, called the JPL GEO-IR Sounder, that would provide profiling of TATM, H_2O, CO, CH_4 and CO_2, as well as numerous other species important for air quality and the hydrological cycle, from a geostationary platform. The JPL GEO-IR Sounder is an imaging Fourier transform spectrometer that utilizes high-speed digital focal plane arrays to record simultaneous TIR and SWIR spectra from each pixel of the array (640 ×480 or 1024×1024 format). The primary advantages of this sounder include the following:

- Coincident spatial and temporal retrievals of trace gases and TATM using both SWIR and TIR bands multiple times per day
- Combined TIR and SWIR retrievals provide for enhanced vertical resolution with PBL visibility for TATM, humidity and multiple trace gases
- Capability for retrievals of 4-D winds from combinations of TATM and H_2O temporal imagery as recently described using GIIRS data (*Ma et al.*, 2021; *Yin et al.*, 2021)
- Providing data products that are not readily obtained by combining retrievals from PoR LEO and GEO sounders.

This paper is organized as follows: in Section 2, we describe the scenarios used in the simulations. Section 3 provides brief descriptions of the radiative transfer (RT), instrument and inverse models. We discuss the considerations imposed on simulated JPL GEO-IR Sounder retrievals in Section 4. In Section 5, we present results for TATM, H_2O and trace gas retrievals from simulated GEO-IR Sounder measurements for both individual spectral regions and combinations. The relevance of these simulated retrievals for Observation System Simulation Experiments is discussed in Section 6. We arrive at some preliminary conclusions in Section 7. In particular, we show that the JPL GEO-IR Sounder would, for the first time, enable high spatial and temporal resolution simultaneous retrievals in the TIR and SWIR,

99 which together provide more vertical profile information and improved sensitivity to the PBL than either

100 spectral region alone.

101

102 **2 Scenarios**

103   Representative atmospheric conditions, including TATM, H_2O and pollutant distributions, surface

104 temperature and other interferents are needed to understand satellite instrument performance. Using

105 Weather Research and Forecasting model coupled to Chemistry (WRF-Chem) simulations at 4 km spatial

106 resolution over the continental United States (Mary Barth, personal communication), we examined about

107 200 atmospheric profiles at six local times for two days in July 2006 over 17 locations that represent a

108 range of diurnal meteorological conditions and a variety of air quality scenarios. For the purposes of

109 these simulations, we assume clear-sky conditions. Simulation of conditions with significant aerosol

110 loading and cloud interference adds significant complexity and is beyond the scope of this study. We

111 calculate molecular absorption coefficients using the Line-By-Line Radiative Transfer Model

112 (LBLRTM; *Clough et al.*, 2005).

113   The main goal of these simulations is to evaluate the retrieval characteristics of TATM, H_2O, and

114 trace gases for different instrument configurations. From our database of over 200 summer-time

115 atmospheric profiles over the continental US, we selected two representative daytime atmospheres; one

116 near Houston to support the weather-focused Observation System Simulation Experiment (OSSE)

117 analyses and the background trace gas case, and another in West Virginia that has more enhanced trace

118 gas pollutants near the surface. Note that we kept the solar and viewing geometry as well as the surface

119 albedo constant in order to isolate the effects of different boundary layer trace gas concentrations. Figure

120 1 shows the profile plots for TATM, H_2O, and trace gases that we examine in this manuscript (O_3, CO,

121 CH_4 and CO_2) at the two locations.

122   The emissivity is obtained from a database structured by month and latitude/longitude coordinates. To

123 populate the database, we used a global land use and land cover classification system developed by the

124 U.S. Geological Survey (*Anderson et al.*, 1976) and mapped them into spectra from the ECOSTRESS

125 spectral library (*Baldridge et al.*, 2009; *Meerdink et al.*, 2019; http://speclib.jpl.nasa.gov/), as described

126 in the TES Algorithm Theoretical Basis Document (*Beer et al.*, 2002). The albedo is calculated from the

127 emissivity using Kirchoff's law.

128   The location and times of the WRF-Chem profiles were used to calculate the solar viewing geometry,

129 assuming a geostationary satellite at 95 W. The NOAA solar position calculator was used to verify the

130 solar zenith and solar azimuth calculations (http://www.srrb.noaa.gov/highlights/sunrise/azel.html).

131

3 Models

3.1 Radiative transfer model

We use the accurate and numerically efficient two-stream-exact-single-scattering (2S-ESS) RT

model (*Spurr and Natraj*, 2011; *Xi et al.*, 2015). This forward model is different from a typical two-

stream model in that the two-stream approximation is used only to calculate the contribution of multiple

scattering to the radiation field. Single scattering is treated in a numerically exact manner using all

moments of the scattering phase function. High computational efficiency is achieved by employing the

two-stream approximation for multiple scattering calculations. The exact single scattering calculation

largely eliminates biases due to the severe truncation of the phase function inherent in a traditional two-

stream approximation. Therefore, the 2S-ESS model is much more accurate than a typical two-stream

model, and produces radiances and Jacobians that are typically within a few percent of numerically exact

calculations and in most cases with biases much less than a percent. This model has been widely used

for the remote sensing of greenhouse gases and aerosols (*Xi et al.*, 2015; *Zhang et al.*, 2015, 2016; *Zeng*

et al., 2017, 2018). Aerosols are not included in the analysis since the main objective was to investigate

the impact of combining multiple spectral bands and of varying instrument parameters. However, the RT

model has the capability of handling generic aerosol types.

The 2S-ESS RT model is used to generate monochromatic radiances at the top of the atmosphere

for the atmospheric profiles and surface conditions near Houston over the entire spectral range considered

for the JPL GEO-IR Sounder. Figure 2 shows the spectral radiance computed on a 0.002 cm^{-1} wavelength

grid. We also calculate the individual contributions of each absorbing gas to the radiance. The gaseous

absorption features have different spectral distributions and line strengths, which can be used to identify

spectral windows for profile retrievals and recognize interfering gases that also absorb strongly in the

same channels.

3.2 Instrument model

This section starts with a brief description of the spectrometer, primarily to define the terms used in

the instrument model. We then detail the focal plane arrays and the optical filter that determine the

bandpasses of the instrument. The processing steps of the instrument model are then explained. Finally,

we show some of the resulting spectra produced by the model.

3.2.1 Optics Overview

The JPL GEO IR Sounder uses a Michelson interferometer, which modulates the light that passes

through it. The interferometer is characterized by two main parameters: the spectral resolution, which is

directly proportional to the maximum optical path difference (MOPD) between the two arms of the

interferometer, and the optical throughput or étendue, which is given by the product of the area of the

165 aperture stop and the angular field of view (AΩ). From geostationary orbit, a ground pixel of 2.1 km

166 subtends an angle of 58.7 μrad and for a Focal Plane Array (FPA) of 1024×1024 pixels, the overall FOV

167 is 60 mrad; this fits well within the Fourier Transform Spectrometer (FTS) design parameters. In parallel

168 with the light from the target scene, a beam from an internal metrology laser travels through the

169 interferometer. This laser is used to precisely measure the optical path difference, to within a small

170 fraction of the laser wavelength. An imaging FTS (IFTS) shares many of the principles of the traditional

171 FTS, the main difference is that the detector is replaced with an FPA. The main challenge in the IFTS

172 design is in the FPA, which must operate at high frame rate (0.5–1 kHz) and at high dynamic range (14–

173 16 bits) to properly digitize the interferograms.

174 *3.2.2 Focal Plane Arrays*

175 The JPL GEO-IR Sounder FPA optics uses a dichroic to split the interferometer output along the

176 wavelength dimension: radiation from 1 μm to 5.3 μm is sent towards FPA #1 and radiation from 5.3 μm

177 to 15.4 μm is directed to FPA #2. Whereas FPA #2 is a single-color detector, handling its full domain at

178 all times, FPA #1 is a dual-color detector. The two colors of FPA #1 are operated sequentially: recording

179 either the 1 μm to 3 μm domain (SWIR; FPA #1a) or the 3 μm to 5.3 μm domain (MWIR; FPA #1b).

180 This dual-color operation is implemented inside the FPA by having two distinct detectors in an optical

181 "sandwich". It is designed to minimize the effect of photon noise in the low-light MWIR and SWIR

182 domains. Furthermore, the SWIR FPA #1a bandpass is narrowed by a triple-band optical filter, tailored

183 to the regions that contain absorption bands of interest (Figure 3). As listed in Table 3, the SWIR domains

184 of interest are: (1) 4210–4350 cm^{-1}, (2) 4810–4900 cm^{-1}, (3) 6000–6150 cm^{-1} and (4) 6170–6290 cm^{-1}.

185 Based on previous optical filter studies, we allow 200 cm^{-1} for the filter slope on either side. Since the

186 gap between the first two domains would therefore be small, and the signal there is low, these have been

187 merged (4210–4900 cm^{-1}). Domains (3) and (4) have also been combined (6000–6290 cm^{-1}). In addition,

188 the 1.27 μm oxygen band (7780–8010 cm^{-1}) will be used to measure the light path. We believe that it is

189 best to specify the 50% transmission points for the filter bands, as that is where the slope is maximum

190 and hence most easily verified. With a 200 cm^{-1} transition region, the 50% point will be 100 cm^{-1} outside

191 of the bandpasses. Hence the final triple-band filter configuration is: 4110–5000 cm^{-1} (2.000–2.433 μm),

192 5900–6390 cm^{-1} (1.565–1.695 μm), 7680–8110 cm^{-1} (1.233–1.302 μm). The triple-band filter physically

193 covers the two-color FPA #1. It is intended to limit the photon flux only in the SWIR mode of operation,

194 with the detector that is sensitive over the 1–3 μm domain (FPA #1a). The filter must also be transparent

195 over the 3–5.3 μm domain of the other shared detector (FPA #1b). It may be possible to combine the

196 first band of the triple-band filter (2–2.433 μm) with this MWIR transparency need (3–5.3 μm) but this

197 has not been simulated in this study.

6

3.2.3 Instrument Model Description

199   The Instrument Model for the JPL GEO IR Sounder allows us to explore the instrument trade space

200   and its effect on retrieved atmospheric composition. It includes the ability to convolve synthetic spectra

201   and Jacobians with the instrument line shape (ILS). The model performs the following steps:

202   1. Reads synthetic data from the radiative transfer model. The radiance spectrum is extended using

203   blackbody curves simulating the Earth and the Sun, and converted to a photon flux spectrum. After this

204   step, the spectrum is in units of photons/m^2/sr/cm^{-1}/s.

205   2. Convolves the spectrum with the theoretical FTS ILS, given as: 2Lsinc(2σL), where L is the MOPD

206   and sinc(x)=sin(πx)/πx. This expression of the ILS has unit area, and hence the convolution does not

207   change the overall magnitude or the units of the spectrum. It does, however, reduce the spectral resolution,

208   broadening all sharp features. In the same step, we resample the spectrum on a coarser grid, i.e., we

209   "decimate" the spectrum. For example, in the current simulations, we reduce the wavenumber interval

210   by a factor of 50, from 0.002 cm^{-1} to 0.1 cm^{-1}.

211   3. Scales the spectrum by the étendue of the instrument. After this step, the units of the spectrum are

212   photons/cm^{-1}/s.

213   4. Applies further scaling to account for the single output design (where half the light is sent through the

214   instrument and the other half sent back to the source), losses in the metallic coatings and at the uncoated

215   optical interfaces (i.e., compensator and back side of beamsplitter), the efficiency of the beamsplitter

216   coating, the quantum efficiency of the detector, and the integration time of the analog-to-digital converter.

217   After this step, the units of the spectrum are photoelectrons/cm^{-1}.

218   5. Applies bandpass limits caused either by an optical filter or the working domain of the detector.

219   6. Applies the Fourier transform to convert the spectrum into an interferogram.

220   7. Computes the number of photoelectrons counted in each interferogram data sample. From this, we can

221   compute the photon noise. Subsequently, white noise is added to the interferogram with a root mean

222   square amplitude matching the computed photon noise.

223   8. Simulates the interferogram digitization, performed for each pixel within the Read Out Integrated

224   Circuit of the two FPAs.

225   9. Produces the final spectrum by Fourier transform. The signal to noise ratio (SNR) is then evaluated

226   by computing the noise level in blacked-out regions on either side of the instrument bandpass, and by

227   locating the maximum signal within the bandpass.

228   *3.2.4 Spectral Results*

229   Figure 3 shows a JPL GEO-IR Sounder model spectrum for FPA #1a, covering the SWIR domain.

230   Figure 4 shows a similar spectrum for the VLWIR, LWIR and MWIR FPA bands: FPA #2 covers the

231   VLWIR and LWIR domains, and FPA #1b covers the MWIR domain. The spectral ranges include the

232   range utilized by existing TIR sounders (AIRS, CrIS, IASI) and selected bands in the SWIR. In particular,

233   the FPA #2 spectral range contains critical information for radiance assimilation by weather forecasting

234   algorithms (see, e.g., *Eresmaa et al.*, 2017). The spectral resolution (MOPD) of the JPL GEO-IR Sounder

235   is configurable. For these simulations, we choose to look at three possible MOPD options: a CrIS-like

236   spectral resolution (0.8 cm MOPD, 0.625 cm^{-1} resolution, described as nominal spectral resolution or

237   NSR in Table 4), an intermediate option (2 cm MOPD, 0.25 cm^{-1} resolution), and a high spectral

238   resolution option (5 cm MOPD, 0.1 cm^{-1} resolution, described as full spectral resolution or FSR in Table

239   4). In order to make for an "apples to apples" comparison, we consider the same integration time (1

240   millisecond per interferogram point) for these three options. The integration time is driven by the high

241   spectral resolution option. The native and binned (footprint-averaged) ground sampling distance (GSD)

242   are also indicated in Table 4.

243   **3.3 Inverse model**

244   We use an optimal estimation approach (*Rodgers*, 2000) and perform linear retrievals from

245   simulated radiances described in the previous section. The spectral differences of the modeled and the

246   satellite measured radiances and the differences of the species profile and the *a priori* profile are

247   mathematically minimized, weighted by the measurement error and the *a priori* constraint. The species

248   profile can then be derived optimally.

249   The *a priori* constraint vectors for TATM and H_2O are obtained from forecast fields from the NASA

250   Global Modeling and Assimilation Office, supplied for use within the TES retrieval algorithm (*Bowman*

251   *et al.*, 2006). *A priori* constraint matrices are constructed, using the method described in *Kulawik et al.*

252   (2006), from an altitude-dependent combination of zeroth, first and second order derivatives of the

253   profiles. For TATM and H_2O, the square roots of the diagonals of the respective constraint matrices are

254   on the order of 1.8–2.2 K and 15–18%, respectively. *A priori* vectors for O_3, CO and CH_4 are taken from

255   calculations using the Model for OZone And Related chemical Tracers (MOZART3) (*Brasseur et al.*,

256   1998; *Park et al.*, 2004) that were performed for the purpose of construction of trace gas climatologies

257   for the Aura mission. For O_3, the square root of the diagonal of the constraint matrix is on the order of

258   25% in the troposphere, 40% in the stratosphere and 15% above. For CO, this is set to 30% over the

259   entire atmosphere, while for CH_4, the values range from 2–10%. The constraint matrices for CO are the

260   same as those used by the MOPITT algorithm (*Deeter et al.*, 2010). For CO_2, the *a priori* vector and

261   constraint used are described in *Kulawik et al.* (2010). The square root of the diagonal of the constraint

262   matrix ranges from 1.2–2%. We note that these profile constraints were developed for TIR instruments,

263   and may therefore not capture strong near-surface variability. There could be scope for increasing the

8

264 near-surface information content via development of updated constraints, although that work is outside

265 of the scope of this study.

266   The end-to-end retrieval analysis provides averaging kernels, which describe the sensitivity of the

267 retrieved atmospheric state to the true state; degrees of freedom for signal (DOFS), which denote the

268 pieces of vertical information contained in the retrieved profile; and retrieval errors. These metrics are

269 used for evaluating the retrieval results for a variety of spectral bands, and spectral and spatial resolutions.

270

271 **4 Considerations for simulated retrievals**

272   For the retrieval simulations described here, we consider a somewhat idealized scenario.

273 Simulations have been performed for clear-sky, no-aerosol conditions. In retrievals from actual measured

274 radiances, even for a clear-sky, non-scattering atmosphere, there is always some forward model error

275 due to, e.g., uncertainties in spectroscopy, interfering species and the treatment of the surface. With real

276 data, these kinds of uncertainties can lead to significant systematic errors in the retrievals, particularly

277 for well-mixed greenhouse gases such as CH_4 and CO_2. For the simulations presented here, we have

278 considered only the error term associated with measurement noise.

279   The measurement noise associated with the simulated radiance is obtained using the instrument

280 model described in Section 3.2. The JPL GEO-IR sounder concept is configurable in terms of spectral

281 range and spectral resolution, with a native spatial resolution that corresponds to a 2.1 km footprint on

282 the ground. Different configurations of the instrument concept will affect the number of photons

283 available in each channel and therefore impact the signal to noise. For a given integration time, lower

284 spectral resolution leads to correspondingly higher SNR. The SNR of the observed radiance spectra can

285 be increased by increasing the integration time. For geostationary observations, this leads to a trade-off

286 between measurement noise and temporal resolution. An increase of the throughput (etendue) leads to

287 lower noise (*Schwantes et al.*, 2002).

288   In retrievals from real data, higher spectral resolution can offer advantages in terms of ability to

289 distinguish between the target molecule and interfering spectral signatures from other molecules with

290 features in the spectral range of interest, despite the increase in measurement noise. In the results

291 presented in this study, that advantage in reduction of systematic error is not accounted for. The SNR

292 can also be increased by aggregating spatially. For example, aggregating four 2.1 km footprints would

293 increase the SNR by a factor of two. Depending on the application of the measurements, there may be

294 some advantage to trading spatial resolution for a gain in SNR.

295

296 **5 Results**

9

5.1 TATM and H_2O retrievals

High spectral resolution is necessary to provide the vertically resolved TATM and H_2O information critical for numerical weather prediction and for many other applications including local extreme weather conditions and global climate change. Current satellite-based TATM and H_2O retrievals mainly utilize TIR spectral measurements. Here we also examine information gained from adding SWIR measurements. Tables 5 and 6 list the possible choices of frequency range for TATM and H_2O retrievals. Some of these spectral ranges are used in current operational missions, while some are candidates for future missions. We compare results for three values of spectral resolution and for two values of spatial resolution.

Examining the above DOFS tables, we see competing effects of spectral resolution (MOPD) and measurement noise. As described in Section 3.2, the measurement noise (Noise Equivalent Spectral Radiance, NESR) is estimated for a fixed integration time for both the 2.1 and 4.2 km ground sampling distance (GSD) configurations. The NESR for the MOPD = 0.8 cm instrument is therefore smaller than that for the MOPD = 2 or 5 cm instruments. Typically, however, the higher spectral resolution instruments provide larger DOFS than the NSR instrument. For H_2O retrievals, the optimal DOFS are provided by the intermediate resolution instrument.

The differences in DOFS for the two GSD values are obvious. This shows the trade-off between spatial resolution and retrieval vertical resolution and precision (not listed). Both GSDs provide high precision, high vertical resolution TATM and H_2O retrievals. We estimate the tropospheric vertical resolution for TATM to be 1.5–2 km with <0.5 K precision, and for H_2O to be 1–2 km with ~5% precision. In comparison, representative tropospheric values for AIRS are 1 km for TATM and 2 km for H_2O (*Irion et al.*, 2018).

The selection of spectral regions also affects the TATM and H_2O products. For example, using the VLWIR+LWIR+MWIR domain provides much more sensitivity compared to using MWIR alone. Figure 5 shows averaging kernel plots for TATM and H_2O for the 4.2 km GSD option for four spectral band combinations: VLWIR+LWIR, MWIR, SWIR, and VLWIR+LWIR+MWIR+SWIR. The characteristics of the TIR TATM and H_2O retrievals are very similar to those obtained by currently operating instruments. We note that the sensitivity of SWIR retrievals is mostly near the surface. Further, the measurement noise in the SWIR was reduced by a factor of 5 in these figures by averaging 25 pixels, thereby reducing the effective GSD to 21 km. Note that this is worse than the 15 km AIRS/CrIS native resolution but better than the 45 km that the TATM and H_2O products are typically reported on. Further, while 5×5 pixels may be required for trace gas retrievals in the SWIR (see section 5.2) and is therefore a little worse than AIRS/CrIS, we measure TIR and SWIR at the same time, eliminating bias from observing with separate instruments.

10

5.2 Trace gas retrievals

Among many possible detectable trace gases from the extended spectral radiance measurements, we selected to examine profile retrieval characteristics for O_3, CO, CH_4 and CO_2 for the given instrument configurations (see Table 3 for retrieval spectral ranges). Table 7 lists DOFS for the chosen trace gases for the West Virginia scenario. Results for the FSR option are largely similar to those for the intermediate spectral resolution instrument and are hence not shown. The DOFS in Table 7 are broadly consistent with previously published work on species profile retrievals from satellite observations (*Beer*, 2006; *Connor et al.*, 2008; *Deeter et al.*, 2009, 2015; *George et al.*, 2009; *Kulawik et al.*, 2010; *Worden et al.*, 2010, 2013; *Clerbaux et al.*, 2015; *Fu et al.*, 2016; *Smith and Barnet*, 2020). For a given spectral resolution instrument, the higher DOFS in retrievals for the larger GSD case for all species are due to the reduced measurement noise. For a given GSD, the DOFS are slightly higher for the NSR case compared to the MOPD = 2 cm case, but the differences are small. It is worth reiterating that these simulated retrievals represent an idealized scenario, where we assume perfect knowledge of interfering species in the spectral range for any given target species. In this scenario, with a constant integration time, the NSR option provides similar results to the MOPD = 2 cm option due to the trade-off between spectral resolution and instrument noise.

Figure 6 shows averaging kernel plots for CO for MWIR- and SWIR-only scenarios and for combined MWIR+SWIR retrievals. The combination of wavelength regions provides improved sensitivity to the lower troposphere compared to either spectral region alone. CO_2 retrievals (Figure 7) benefit the most from the combination of VLWIR+MWIR+SWIR retrievals. The SWIR domain adds sensitivity in the lower troposphere and near the surface. The characteristics of the CO_2 retrievals are in good agreement with OCO-2/3 observations. For CH_4 (Figure 8), the addition of SWIR bands also provides noticeable enhancement in lower tropospheric and near-surface sensitivity. For CO retrievals, the contribution of the SWIR to the near-surface sensitivity is less pronounced. The stronger contribution of SWIR measurements to the total DOFS for CH_4 and CO_2 compared to CO is a result of three factors: (1) lower top of the atmosphere solar irradiance in the CO spectral region relative to the CH_4 and CO_2 regions, (2) lower surface albedo, and (3) larger absorption, primarily by H_2O and CH_4. Our results for O_3 are broadly consistent with published results for LWIR satellite observations (e.g., *Nassar et al.*, 2008; *Smith and Barnet*, 2020). Figures 6–8 use the same effective GSD of 21 km in the SWIR as described in Section 5.1.

6 Discussion: Use of GEO-IR Information in Data Assimilation and Observation System Simulation Experiments

11

363   We have focused in this paper on the characteristics of the measurements and retrievals that we

364   expect to obtain from the GEO-IR observing platform. While this paper does not deal directly with the

365   use of this information in a data assimilation system, the results we have presented lay the necessary

366   groundwork for future work in this area. In particular, the detailed characterization of uncertainties in the

367   TATM and H_2O retrievals provided by this study can be directly incorporated into a set of weather

368   forecast OSSEs. We have begun this research, and will report on the results in a subsequent paper. Note

369   that, for a weather forecast OSSE to be credible, it is crucial to represent the synthetic measurements as

370   accurately as possible. TATM and H_2O precision and total error are reported in Table 8; it can be seen

371   that the errors for the MWIR-only configuration are on the order of the errors in CrIS and AIRS retrievals,

372   while the full-spectrum JPL GEO-IR Sounder configuration yields total errors that are smaller than those

373   from either CrIS or AIRS. As such, assimilation of information from JPL GEO-IR Sounder

374   measurements is expected *a priori* to have as much or greater impact on weather forecasts compared

375   with existing hyperspectral sounders. Note that the total error in the full-spectral-range TATM and H_2O

376   retrievals is equivalent to, or less than, the uncertainty reported for radiosonde measurements of these

377   quantities (*Rienecker et al.*, 2008; Table 3.5.2).

378   We also note that there will be particular advantages and challenges in assimilating the high

379   temporal resolution data that will be available from the JPL GEO-IR Sounder. The clear advantage is the

380   ability to observe rapidly evolving processes (e.g., the environment around thunderstorms and hurricanes;

381   see, e.g., *Li et al.*, 2018). This information is not available from the current LEO constellation. However,

382   many modern data assimilation systems are configured for assimilation of intermittent data (at best

383   hourly in operational data assimilation systems). While four-dimensional variational data assimilation

384   (4D-Var) is capable of ingesting data at non-synoptic times, assimilation of sub-hourly data remains

385   challenging. It is likely that all but the most rapid-update data assimilation systems will require

386   modification to make best use of the high time frequency geostationary soundings provided by the JPL

387   GEO-IR Sounder.

388

389 7 Conclusions

390   In this paper, we present an end-to-end retrieval study for a proposed FTS instrument covering the

391   entire infrared spectral range from 1–15 µm from a geostationary satellite orbit. An instrument model is

392   used to derive realistic measurement radiance and noise for several diurnal observations over small

393   ground footprints (e.g., 2.1 km). We perform TATM and trace gas profile retrievals for the JPL GEO-IR

394   Sounder that covers the entire VLWIR, LWIR, MWIR and SWIR spectral domains. Retrieval

395   characteristics, such as DOFS and measurement error, are examined in order to evaluate the performance

396 of several instrument configurations. These configurations include VLWIR-, LWIR-, MWIR-, and

397 SWIR-only and their combinations, and different spectral and spatial resolutions, for a realistic

398 geostationary observing system making field-of-view observations at fixed time intervals. Two summer-

399 time atmospheres are used: a scenario near Houston as a clean-air case, and one in West Virginia

400 representing a polluted scenario. We analyze TATM, H_2O, O_3, CO, CH_4 and CO_2 profile retrievals.

401 High spectral resolution can provide improved ability to distinguish absorption lines of the target

402 species from interferents. In the case of species (such as O_3) where much of the total column lies in the

403 stratosphere, higher spectral resolution also provides enhanced ability to separate the tropospheric signal

404 from the stratospheric signal. When the total integration time is fixed, there is a trade-off between spectral

405 resolution and noise. In the idealized retrievals presented here, we assume perfect knowledge of

406 interfering species. In this case, three different MOPDs provide comparable results in terms of DOFS.

407 However, in the real world, we would expect higher spectral resolution to offer advantages in terms of

408 reduction in systematic errors.

409 Compared to single spectral region instruments, e.g., only LWIR or MWIR, combinations of

410 VLWIR/LWIR/MWIR/SWIR enhance the sensitivity of the retrievals to the lower troposphere. In our

411 analyses, we find that the contributions from the SWIR in the combined measurements are noticeable for

412 both trace gas and TATM retrievals, especially when the ground pixels are averaged to reduce

413 measurement noise in the SWIR. In particular, the SWIR measurements add information in the lower

414 troposphere and for near-surface species retrievals.

415 We limit the spatial resolution choices to GSD = 2.1 km and 4.2 km in our simulations. Especially

416 for multi-band retrievals, the results are realistically adequate for many research applications for both

417 ground sampling footprints. We compare performance metrics (e.g., NESR and SNR) for the proposed

418 instrument with values for several current/past satellite instruments in multiple spectral bands. The

419 performance of the JPL GEO-IR Sounder is similar to or better than currently operational instruments.

420 At the same time, the JPL GEO-IR Sounder provides much higher spatial and temporal resolution and a

421 wider range of trace gases than current instruments that combine TIR and SWIR. The derived retrieval

422 characteristics (e.g., DOFS and retrieval errors) also compare favorably with currently available

423 products.

424

425 **Data availability**

426 The code and data are available from the authors upon request.

427 **Author contributions**

428   SPS, Y-HW and LID conceived the work. VN provided the radiative transfer model, led the
429   simulated retrieval work, and prepared the manuscript. ML, J-FB and ZZ assisted with the retrievals. ML
430   provided the trace gas absorption and inverse models. JLN provided the profiles for the simulations. SSK
431   provided the emissivity database and advised on the retrieval constraints. J-FB provided the instrument
432   model. VHP and SPS helped analyze the simulation results. LW, JAR and DJP provided the connection
433   with OSSEs. All listed authors contributed to the review and editing of this manuscript.
434

References

Adkins, J., Alsheimer, F., Ardanuy, P., Boukabara, S., Casey, S., Coakley, M., Conran, J., Cucurull, L., Daniels, J., Ditchek, S. D., Gallagher, F., Garrett, K., Gerth, J., Goldberg, M., Goodman, S., Grigsby, E., Griffin, M., Griffin, V., Hardesty, M., Iturbide, F., Kalluri, S., Knuteson, R., Krimchansky, A., Lauer, C., Lindsey, D., McCarty, W., McCorkel, J., Ostroy, J., Pogorzala, D., Revercomb, H., Rivera, R., Seybold, M., Schmit, T., Smith, B., Sullivan, P., Talaat, E., Tewey, K., Todirita, M., Tremblay, D., Vassiliadis, D., Weir, P., and Yoe, J.: Geostationary Extended Observations (GeoXO) hyperspectral infrared sounder value assessment report, NOAA Tech. Rep., National Environmental Satellite, Data, and Information Service, https://doi.org/10.25923/7zvz-fv26, 2021.

Anderson, J. R., Hardy, E. E., Roach, J. T., and Witmer, R. E.: A land use and land cover classification system for use with remote sensor data, USGS Tech Rep., https://doi.org/10.3133/pp964, 1976.

Baldridge, A. M., S. J. Hook, C. I. Grove, and G. Rivera: The ASTER spectral library version 2.0, Remote Sens. Environ., 113(4), 711–715, https://doi.org/10.1016/j.rse.2008.11.007, 2009.

Beer, R., Bowman, K. W., Brown, P. D., Clough, S. A., Eldering, A., Goldman, A., Jacob, D. J., Lampel, M., Logan, J. A., Luo, M., Murcray, F. J., Osterman, G. B., Rider, D. M., Rinsland, C. P., Rodgers, C. D., Sander, S. P., Shepard, M., Sund, S., Ustinov, E., Worden, H. M., and Worden, J.: Tropospheric Emission Spectrometer (TES) level 2 algorithm theoretical basis document, Version 1.15, JPL D-16474, Jet Propulsion Laboratory, Pasadena, California (available at https://eospso.gsfc.nasa.gov/atbd-category/53), 2002.

Beer, R.: TES on the Aura mission: Scientific objectives, measurements, and analysis overview, IEEE Trans. Geosci. Remote Sens., 44(5), 1102–1105, https://doi.org/10.1109/TGRS.2005.863716, 2006.

Bowman, K. W., Rodgers, C. D., Kulawik, S. S., Worden, J., Sarkissian, E., Osterman, G., Steck, T., Luo, M., Eldering, A., Shephard, M., Worden, H., Lampel, M., Clough, S., Brown, P., Rinsland, C., Gunson, M., and Beer, R.: Tropospheric Emission Spectrometer: Retrieval method and error analysis, IEEE Trans. Geosci. Remote Sens., 44(5), 1297–1307, https://doi.org/10.1109/TGRS.2006.871234, 2006.

480   Borsdorff, T., Aan de Brugh, J., Hu, H., Aben, I., Hasekamp, O., and Landgraf, J.: Measuring carbon

481   monoxide with TROPOMI: First results and a comparison with ECMWF-IFS analysis data, Geophys.

482   Res. Lett., 45(6), 2826–2832, https://doi.org/10.1002/2018GL077045, 2018.

483

484   Borsdorff, T., aan de Brugh, J., Hu, H., Nédélec, P., Aben, I., and Landgraf, J.: Carbon monoxide column

485   retrieval for clear-sky and cloudy atmospheres: A full-mission data set from SCIAMACHY 2.3 μm

486   reflectance measurements, Atmos. Meas. Tech., 10(5), 1769–1782, https://doi.org/10.5194/amt-10-

487   1769-2017, 2017.

488

489   Brasseur, G. P., Hauglustaine, D. A., Walters, S., Rasch, P. J., Muller, J. F., Granier, C., and Tie, X. X.:

490   MOZART, a global chemical transport model for ozone and related chemical tracers 1. Model

491   description, J. Geophys. Res., 103(D21), 28265–28289, https://doi.org/10.1029/98JD02397, 1998.

492

493   Buchholz, R. R., Worden, H. M., Park, M., Francis, G., Deeter, M. N., Edwards, D. P., Emmons, L. K.,

494   Gaubert, B., Gille, J., Martinez-Alonso, S., Tang, W., Kumar, R., Drummond, J. R., Clerbaux, C.,

495   George, M., Coheur, P.-F., Hurtmans, D., Bowman, K. W., Luo, M., Payne, V. H., Worden, J. R., Chin,

496   M., Levy, R. C., Warner, J., Wei, Z., and Kulawik, S. S.: Air pollution trends measured from Terra: CO

497   and AOD over industrial, fire-prone, and background regions, Remote Sens. Environ., 256, 112275,

498   https://doi.org/10.1016/j.rse.2020.112275, 2021.

499

500   Buchwitz, M., de Beek, R., Bramstedt, K., Noël, S., Bovensmann, H., and Burrows, J. P.: Global carbon

501   monoxide as retrieved from SCIAMACHY by WFM-DOAS, Atmos. Chem. Phys., 4(7), 1945–1960,

502   https://doi.org/10.5194/acp-4-1945-2004, 2004.

503

504   Buchwitz, M., de Beek, R., Noël, S., Burrows, J. P., Bovensmann, H., Bremer, H., Bergamaschi, P.,

505   Körner, S., and Heimann, M.: Carbon monoxide, methane and carbon dioxide columns retrieved from

506   SCIAMACHY by WFM-DOAS: Year 2003 initial data set, Atmos. Chem. Phys., 5(12), 3313–3329,

507   https://doi.org/10.5194/acp-5-3313-2005, 2005.

508

509   Christi, M. J., and Stephens, G. L.: Retrieving profiles of atmospheric CO_2 in clear sky and in the

510   presence of thin cloud using spectroscopy from the near and thermal infrared: A preliminary case study,

511   J. Geophys. Res., 109(D4), D04316, https://doi.org/10.1029/2003jd004058, 2004.

16

512 Clough, S. A., Shephard, M. W., Mlawer, E., Delamere, J. S., Iacono, M., Cady-Pereira, K., Boukabara,

513 S., and Brown, P. D.: Atmospheric radiative transfer modeling: a summary of the AER codes, J. Quant.

514 Spectrosc. Radiat. Transfer, 91(2), 233–244, https://doi.org/10.1016/j.jqsrt.2004.05.058, 2005.

515

516 Connor, B. J., Boesch. H., Toon, G., Sen, B., Miller, C., and Crisp, D.: Orbiting Carbon Observatory:

517 Inverse method and prospective error analysis, J. Geophys. Res., 113, D05305,

518 https://doi.org/10.1029/2006JD008336, 2008.

519

520 Clerbaux, C., Hadji-Lazaro, J., Turquety, S., George, M., Boynard, A., Pommier, M., Safieddine, S.,

521 Coheur, P.-F., Hurtmans, D., Clarisse, L., and Van Damme, M.: Tracking pollutants from space: Eight

522 years of IASI satellite observation, C. R. Géosci., 347(3), 134–144,

523 https://doi.org/10.1016/j.crte.2015.06.001, 2015.

524

525 Deeter, M. N., Edwards, D. P., Gille, J. C., and Drummond, J. R.: CO retrievals based on MOPITT near-

526 infrared observations, J. Geophys. Res., 114(D4), D04303, https://doi.org/10.1029/2008JD010872, 2009.

527

528 Deeter, M. N., Edwards, D. P., Gille, J. C., Emmons, L. K., Francis, G., Ho, S.-P., Mao, D., Masters, D.,

529 Worden, H. M., Drummond, J. R., and Novelli, P. C.: The MOPITT version 4 CO product: Algorithm

530 enhancements, validation, and long-term stability, J. Geophys. Res., 115(D7), D07306,

531 https://doi.org/10.1029/2009JD013005, 2010.

532

533 Deeter, M. N., Edwards, D. P., Gille, J. C., and Worden, H. M.: Information content of MOPITT CO

534 profile retrievals: Temporal and geographical variability, J. Geophys. Res., 120(24), 12723–12738,

535 https://doi.org/10.1002/2015JD024024, 2015.

536

537 Eresmaa, R., Letertre-Danczak, J., Lupu, C., Bormann, N., and McNally, A. P.: The assimilation of

538 Cross-track Infrared Sounder radiances at ECMWF, Q. J. R. Meteorolog. Soc., 143(709), 3177–3188,

539 2017, https://doi.org/10.1002/qj.3171.

540

541 Frankenberg, C., Meirink, J. F., Bergamaschi, P., Goede, A. P. H., Heimann, M., Körner, S., Platt, U.,

542 van Weele, M., and Wagner, T.: Satellite chartography of atmospheric methane from SCIAMACHY on

543 board ENVISAT: Analysis of the years 2003 and 2004, J. Geophys. Res., 111(D7), D07303,

544 https://doi.org/10.1029/2005JD006235, 2006.

545 Fu, D., Bowman, K. W., Worden, H. M., Natraj, V., Worden, J. R., Yu, S., Veefkind, P., Aben, I.,

546 Landgraf, J., Strow, L., and Han, Y.: High-resolution tropospheric carbon monoxide profiles retrieved

547 from CrIS and TROPOMI, Atmos. Meas. Tech., 9(6), 2567–2579, doi:10.5194/amt-9-2567-2016, 2016.

548

549 George, M., Clerbaux, C., Hurtmans, D., Turquety, S., Coheur, P.-F., Pommier, M., Hadji-Lazaro, J.,

550 Edwards, D. P., Worden, H., Luo, M., Rinsland, C., and McMillan, W.: Carbon monoxide distributions

551 from the IASI/METOP mission: Evaluation with other space-borne remote sensors, Atmos. Chem. Phys.,

552 9(21), 8317–8330, https://doi.org/10.5194/acp-9-8317-2009, 2009.

553

554 Holmlund, K., Grandell, J., Schmetz, J., Stuhlmann, R., Bojkov, B., Munro, R., Lekouara, M., Coppens,

555 D., Viticchie, B., August, T., Theodore, B., Watts, P., Dobber, M., Fowler, G., Bojinski, S., Schmid, A.,

556 Salonen, K., Tjemkes, S., Aminou, D., and Blythe, P.: Meteosat Third Generation (MTG): Continuation

557 and innovation of observations from geostationary orbit, Bull. Am. Meteorol. Soc., 102(5), E990–E1015,

558 https://doi.org/10.1175/BAMS-D-19-0304.1, 2021.

559

560 Hu, H., Landgraf, J., Detmers, R., Borsdorff, T., Aan de Brugh, J., Aben, I., Butz, A., and Hasekamp,

561 O.: Toward global mapping of methane with TROPOMI: First results and intersatellite comparison to

562 GOSAT, Geophys. Res. Lett., 45(8), 3682–3689, https://doi.org/10.1002/2018GL077259, 2018.

563

564 Irion, F. W., Kahn, B. H., Schreier, M. M., Fetzer, E. J., Fishbein, E., Fu, D., Kalmus, P., Wilson, R. C.,

565 Wong, S., and Yue, Q.: Single-footprint retrievals of temperature, water vapor and cloud properties from

566 AIRS, Atmos. Meas. Tech., 11(2), 971–995, https://doi.org/10.5194/amt-11-971-2018, 2018.

567

568 Kuai, L., Worden, J., Kulawik, S., Bowman, K., Lee, M., Biraud, S. C., Abshire, J. B., Wofsy, S. C.,

569 Natraj, V., Frankenberg, C., Wunch, D., Connor, B., Miller, C., Roehl, C., Shia, R.-L., and Yung, Y.:

570 Profiling tropospheric CO_2 using Aura TES and TCCON instruments, Atmos. Meas. Tech., 6(1), 63–79,

571 https://doi.org/10.5194/amt-6-63-2013, 2013.

572

573 Kulawik, S. S., Osterman, G., Jones, D.B.A., and Bowman, K.W.: Calculation of altitude-dependent

574 Tikhonov constraints for TES nadir retrievals, IEEE Trans. Geosci. Remote Sens., 44(5), 1334–1342,

575 https://doi.org/10.1109/TGRS.2006.871206,2006.

576

577 Kulawik, S. S., Jones, D. B. A., Nassar, R., Irion, F. W., Worden, J. R., Bowman, K. W., Machida, T.,
578 Matsueda, H., Sawa, Y., Biraud, S. C., Fischer, M. L., and Jacobson, A. R.: Characterization of
579 Tropospheric Emission Spectrometer (TES) CO_2 for carbon cycle science, Atmos. Chem. Phys., 10(12),
580 5601–5623, https://doi.org/10.5194/acp-10-5601-2010, 2010.
581
582 Landgraf, J., Aan de Brugh, J., Scheepmaker, R., Borsdorff, T., Hu, H., Houweling, S., Butz, A., Aben,
583 I., and Hasekamp, O.: Carbon monoxide total column retrievals from TROPOMI shortwave infrared
584 measurements, Atmos. Meas. Tech., 9(10), 4955–4975, https://doi.org/10.5194/amt-9-4955-2016, 2016.
585
586 Li, Z., Li, J., Wang, P., Lim, A., Li, J., Schmit, T. J., Atlas, R., Boukabara, S.-A., and Hoffman, R. N.:
587 Value-added impact of geostationary hyperspectral infrared sounders on local severe storm forecasts—
588 via a quick regional OSSE, Adv. Atmos. Sci., 35(10), 1217–1230, https://doi.org/10.1007/s00376-018-
589 8036-3, 2018.
590
591 Ma, Z., Li, J., Han, W., Li, Z., Zeng, Q., Menzel, W. P., Schmit, T. J., Di, D., and Liu, C.-Y.: Four-
592 dimensional wind fields from geostationary hyperspectral infrared sounder radiance measurements with
593 high temporal resolution, Geophys. Res. Lett., 48(14), e2021GL093794,
594 https://doi.org/10.1029/2021GL093794, 2021.
595
596 Meerdink, S. K., Hook, S. J., Roberts, D. A., and Abbott, E. A.: The ECOSTRESS spectral library version
597 1.0, Remote Sens. Environ., 230(111196), 1–8, https://doi.org/10.1016/j.rse.2019.05.015, 2019.
598
599 Nassar, R., Logan, J. A., Worden, H. M., Megretskaia, I. A., Bowman, K. W., Osterman, G. B.,
600 Thompson, A. M., Tarasick, D. W., Austin, S., Claude, H., Dubey, M. K., Hocking, W. K., Johnson, B.
601 J., Joseph, E., Merrill, J., Morris, G. A., Newchurch, M., Oltmans, S. J., Posny, F., Schmidlin, F. J.,
602 Vomel, H., Whiteman, D. N., and Witte, J. C.: Validation of Tropospheric Emission Spectrometer (TES)
603 nadir ozone profiles using ozonesonde measurements, J. Geophys. Res., 113(D15), D15S17,
604 https://doi.org/10.1029/2007JD008819, 2008.
605
606 National Academies of Sciences, Engineering, and Medicine (NASEM): Thriving on Our Changing
607 Planet: A Decadal Strategy for Earth Observation from Space, The National Academies Press,
608 Washington, DC, https://doi.org/10.17226/24938, 2018.
609

Nelson, R. R., Crisp, D., Ott, L. E., and O'Dell, C. W.: High-accuracy measurements of total column water vapor from the Orbiting Carbon Observatory-2, Geophys. Res. Lett., 43(23), 12261–12269, https://doi.org/10.1002/2016GL071200, 2016.

Noël, S., Buchwitz, M., Bovensmann, H., and Burrows, J. P.: Validation of SCIAMACHY AMC-DOAS water vapour columns, Atmos. Chem. Phys., 5(7), 1835–1841, https://doi.org/10.5194/acp-5-1835-2005, 2005.

O'Dell, C. W., Eldering, A., Wennberg, P. O., Crisp, D., Gunson, M. R., Fisher, B., Frankenberg, C., Kiel, M., Lindqvist, H., Mandrake, L., Merrelli, A., Natraj, V., Nelson, R. R., Osterman, G. B., Payne, V. H., Taylor, T. R., Wunch, D., Drouin, B. J., Oyafuso, F., Chang, A., McDuffie, J., Smyth, M., Baker, D. F., Basu, S., Chevallier, F., Crowell, S. M. R., Feng, L., Palmer, P. I., Dubey, M., García, O. E., Griffith, D. W. T., Hase, F., Iraci, L. T., Kivi, R., Morino, I., Notholt, J., Ohyama, H., Petri, C., Roehl, C. M., Sha, M. K., Strong, K., Sussmann, R., Te, Y., Uchino, O., and Velazco, V. A.: Improved retrievals of carbon dioxide from the Orbiting Carbon Observatory-2 with the version 8 ACOS algorithm, Atmos. Meas. Tech., 11(12), 6539–6576, https://doi.org/10.5194/amt-2018-257, 2018.

Park, M., Randel, W. J., Kinnison, D. E., Garcia, R. R., and Choi, W.: Seasonal variation of methane, water vapor, and nitrogen oxides near the tropopause: Satellite observations and model simulations, J. Geophys. Res., 109(D3), https://doi.org/10.1029/2003JD003706, 2004.

Parker, R. J., Webb, A., Boesch, H., Somkuti, P., Barrio Guillo, R., Di Noia, A., Kalaitzi, N., Anand, J. S., Bergamaschi, P., Chevallier, F., Palmer, P. I., Feng, L., Deutscher, N. M., Feist, D. G., Griffith, D. W. T., Hase, F., Kivi, R., Morino, I., Notholt, J., Oh, Y.-S., Ohyama, H., Petri, C., Pollard, D. F., Roehl, C., Sha, M. K., Shiomi, K., Strong, K., Sussmann, R., Té, Y., Velazco, V. A., Warneke, T., Wennberg, P. O., and Wunch, D.: A decade of GOSAT proxy satellite CH_4 observations, Earth Syst. Sci. Data, 12(4), 3383–3412, https://doi.org/10.5194/essd-12-3383-2020, 2020.

Rienecker, M. M., Suarez, M. J., Todling, R., Bacmeister, J., Takacs, L., Liu, H.-C., Gu, W., Sienkiewicz, M., Koster, R. D., Gelaro, R., Stajner, I., and Nielsen, J. E.: The GEOS-5 Data Assimilation System— Documentation of Versions 5.0.1, 5.1.0, and 5.2.0, NASA Tech. Rep. NASA/TM-2008-104606, 27, 2008.

642 Rodgers, C. D.: Inverse Methods for Atmospheric Sounding: Theory and Practice, World Scientific,
643 Singapore, 2000.

645 Schmit, T. J., Li, J., Ackerman, S. A., and Gurka, J. J.: High-spectral- and high-temporal-resolution
646 infrared measurements from geostationary orbit, J. Atmos. Oceanic Technol., 26(11), 2273–2292,
647 https://doi.org/10.1175/2009JTECHA1248.1, 2009.

649 Schneider, M., Ertl, B., Diekmann, C. J., Khosrawi, F., Röhling, A. N., Hase, F., Dubravica, D., García,
650 O. E., Sepúlveda, E., Borsdorff, T., Landgraf, J., Lorente, A., Chen, H., Kivi, R., Laemmel, T., Ramonet,
651 M., Crevoisier, C., Pernin, J., Steinbacher, M., Meinhardt, F., Deutscher, N. M., Griffith, D. W. T.,
652 Velazco, V. A., and Pollard, D. F.: Synergetic use of IASI and TROPOMI space borne sensors for
653 generating a tropospheric methane profile product, Atmos. Meas. Tech. Discuss. [preprint],
654 https://doi.org/10.5194/amt-2021-31, in review, 2021.

656 Schwantes, K. R., Cohen, D., Mantica, P., and Glumb, R. J.: Modeling noise equivalent change in
657 radiance (NEdN) for the Crosstrack Infrared Sounder (CrIS), Proc. SPIE, 4486, 456–463,
658 https://doi.org/10.1117/12.455128, 2002.

660 Smith, N., and Barnet, C. D.: CLIMCAPS observing capability for temperature, moisture, and trace gases
661 from AIRS/AMSU and CrIS/ATMS, Atmos. Meas. Tech., 13(8), 4437–4459,
662 https://doi.org/10.5194/amt-13-4437-2020, 2020.

664 Spurr, R., and Natraj, V.: A linearized two-stream radiative transfer code for fast approximation of
665 multiple-scatter fields, J. Quant. Spectrosc. Radiat. Transfer, 112(16), 2630–2637,
666 https://doi.org/10.1016/j.jqsrt.2011.06.014, 2011.

668 Teixeira, J., Piepmeier, J. R., Nehrir, A. R., Ao, C. O., Chen, S. S., Clayson, C. A., Fridlind, A. M.,
669 Lebsock, M., McCarty, W., Salmun, H., Santanello, J. A., Turner, D. D., Wang, Z., and Zeng, X.: Toward
670 a Global Planetary Boundary Layer Observing System, https://science.nasa.gov/science-pink/s3fs-
671 public/atoms/files/NASAPBLIncubationFinalReport.pdf.

673 Trent, T., Boesch, H., Somkuti, P., and Scott, N. A.: Observing water vapour in the planetary boundary
674 layer from the short-wave infrared, Remote Sens., 10(9), 1469, https://doi.org/10.3390/rs10091469, 2018.

675   Worden, H. M., Deeter, M. N., Edwards, D. P., Gille, J. C., Drummond, J. R., and Nédélec, P. P.:

676   Observations of near-surface carbon monoxide from space using MOPITT multispectral retrievals, J.

677   Geophys. Res., 115(D18), D18314, https://doi.org/10.1029/2010JD014242, 2010.

678

679   Worden, H. M., Deeter, M. N., Frankenberg, C., George, M., Nichitiu, F., Worden, J., Aben, I., Bowman,

680   K. W., Clerbaux, C., Coheur, P. F., de Laat, A. T. J., Detweiler, R., Drummond, J. R., Edwards, D. P.,

681   Gille, J. C., Hurtmans, D., Luo, M., Martínez-Alonso, S., Massie, S., Pfister, G., and Warner, J. X.:

682   Decadal record of satellite carbon monoxide observations, Atmos. Chem. Phys., 13(2), 837–850,

683   https://doi.org/10.5194/acp-13-837-2013, 2013.

684

685   Worden, J. R., Turner, A. J., Bloom, A., Kulawik, S. S., Liu, J., Lee, M., Weidner, R., Bowman, K.,

686   Frankenberg, C., Parker, R., and Payne, V. H.: Quantifying lower tropospheric methane concentrations

687   using GOSAT near-IR and TES thermal IR measurements, Atmos. Meas. Tech., 8(8), 3433–3445,

688   https://doi.org/10.5194/amt-8-3433-2015, 2015.

689

690   Xi, X., Natraj, V., Shia, R.-L., Luo, M., Zhang, Q., Newman, S., Sander, S. P., and Yung, Y. L.:

691   Simulated retrievals for the remote sensing of CO_2, CH_4, CO, and H_2O from geostationary orbit, Atmos.

692   Meas. Tech., 8(11), 4817–4830, https://doi.org/10.5194/amt-8-4817-2015, 2015.

693

694   Yang, J., Zhang, Z., Wei, C., Lu, F., and Guo, Q.: Introducing the new generation of Chinese

695   geostationary weather satellites, Fengyun-4, Bull. Am. Meteorol. Soc., 98(8), 1637–1658,

696   https://doi.org/10.1175/BAMS-D-16-0065.1, 2017.

697

698   Yin, R., Han, W., Gao, Z., and Li, J.: Impact of high temporal resolution FY-4A Geostationary

699   Interferometric Infrared Sounder (GIIRS) radiance measurements on typhoon forecasts: Maria (2018)

700   case with GRAPES global 4D-Var assimilation system, Geophys. Res. Lett., 48(15), e2021GL093672,

701   https://doi.org/10.1029/2021GL093672, 2021.

702

703   Yokota, T., Yoshida, Y., Eguchi, N., Ota, Y., Tanaka, T., Watanabe, H., and Maksyutov, S.: Global

704   concentrations of CO_2 and CH_4 retrieved from GOSAT: First preliminary results, Sci. Online Lett.

705   Atmos., 5(1), 160–163, https://doi.org/10.2151/sola.2009-041, 2009.

706

707   Zeng, Z.-C., Natraj, V., Xu, F., Pongetti, T. J., Shia, R.-L., Kort, E. A., Toon, G. C., Sander, S. P., and

708   Yung, Y. L.: Constraining aerosol vertical profile in the boundary layer using hyperspectral

709   measurements of oxygen absorption, Geophys. Res. Lett., 45(19), 10772–10780,

710   https://doi.org/10.1029/2018gl079286, 2018.

711

712   Zeng, Z.-C., Zhang, Q., Natraj, V., Margolis, J. S., Shia, R.-L., Newman, S., Fu, D., Pongetti, T. J., Wong,

713   K. W., Sander, S. P., Wennberg, P. O., and Yung, Y. L.: Aerosol scattering effects on water vapor

714   retrievals over the Los Angeles Basin, Atmos. Chem. Phys., 17(4), 2495–2508,

715   https://doi.org/10.5194/acp-17-2495-2017, 2017.

716

717   Zhang, Q., Natraj, V., Li, K.-F., Shia, R.-L., Fu, D., Pongetti, T. J., Sander, S. P., Roehl, C. M., and Yung,

718   Y. L.: Accounting for aerosol scattering in the CLARS retrieval of column averaged CO_2 mixing ratios,

719   J. Geophys. Res., 120(14), 7205–7218, https://doi.org/10.1002/2015jd023499, 2015.

720

721   Zhang, Q., Shia, R.-L., Sander, S. P., and Yung, Y. L.: XCO_2 retrieval error over deserts near critical

722   surface albedo, Earth Space Sci., 3(2), 36–45, https://doi.org/10.1002/2015ea000143, 2016.

723

724   Zhang, Y., Jacob, D. J., Maasakkers, J. D., Sulprizio, M. P., Sheng, J.-X., Gautam, R., and Worden, J.:

725   Monitoring global tropospheric OH concentrations using satellite observations of atmospheric methane,

726   Atmos. Chem. Phys., 18(21), 15959–15973, https://doi.org/10.5194/acp-18-15959-2018, 2018.
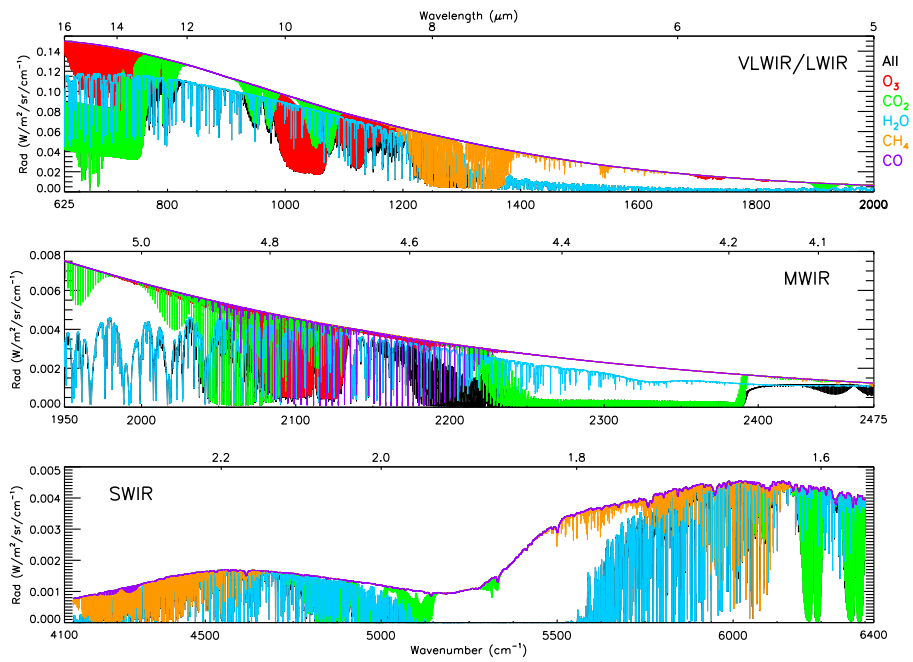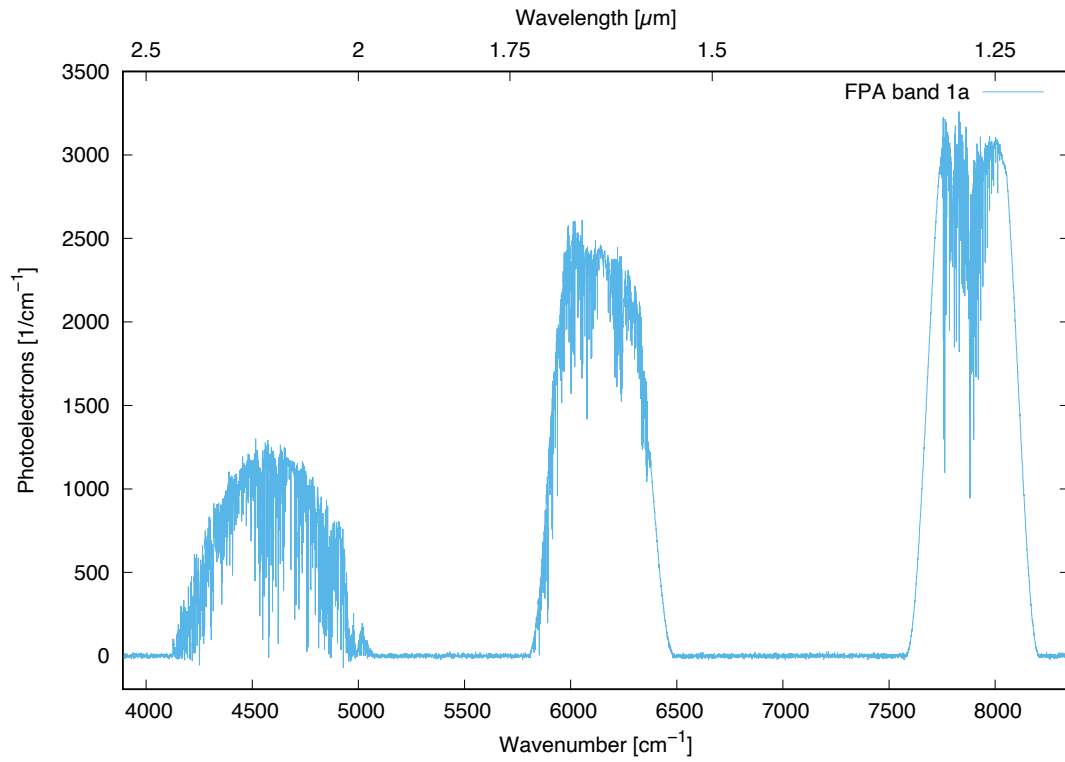
727

728
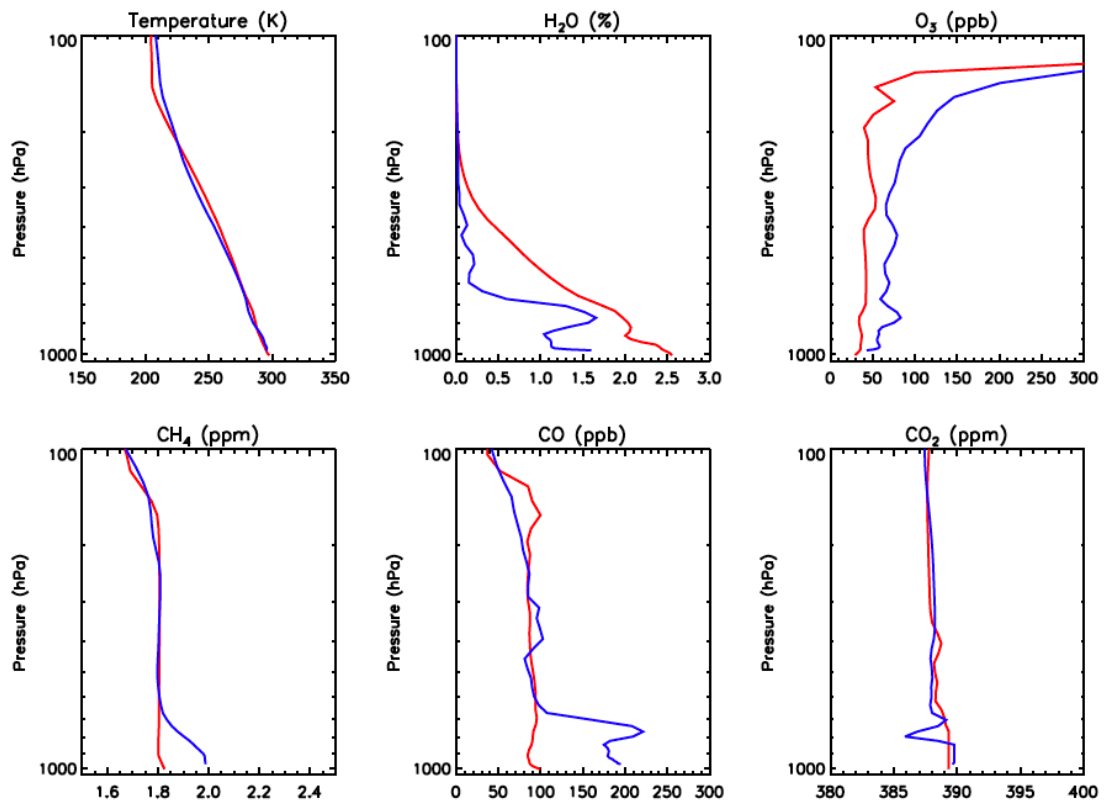
Figure 1: Scenarios considered in the simulations.

729

730

Figure 2. Simulated top of the atmosphere monochromatic radiances (black) in the 650–7000 cm⁻¹ wavelength range for atmospheric profile near Houston. Also shown are radiances corresponding to (red) O_3, (green) CO_2, (blue) H_2O, (orange) CH_4, and (purple) CO absorption.

736

Figure 3: Simulated JPL GEO-IR Sounder spectrum in the SWIR domain. The SWIR domain is sub-divided
into discrete bands using a triple-band interference filter to maximize the SNR in spectral regions of interest
(CO_2, CH_4, CO, H_2O, and O_2).

740

741
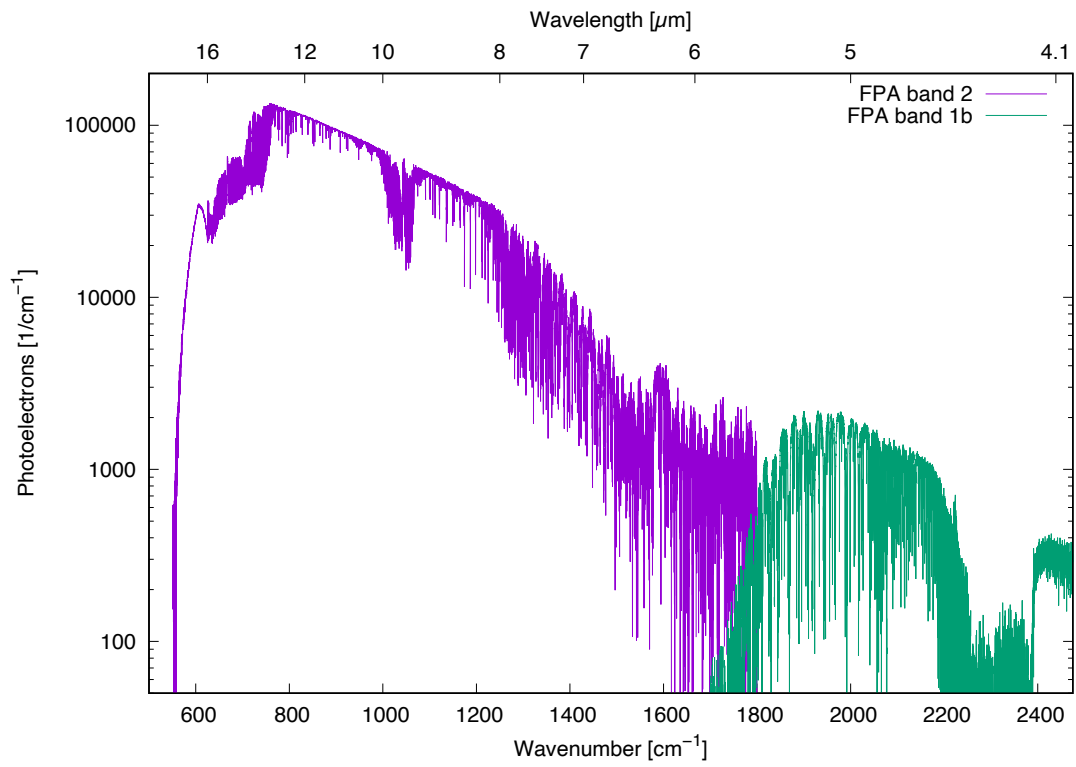
Figure 4: Simulated JPL GEO-IR Sounder spectrum in the VLWIR, LWIR and MWIR domains. Note the

logarithmic scale.

742

743

744
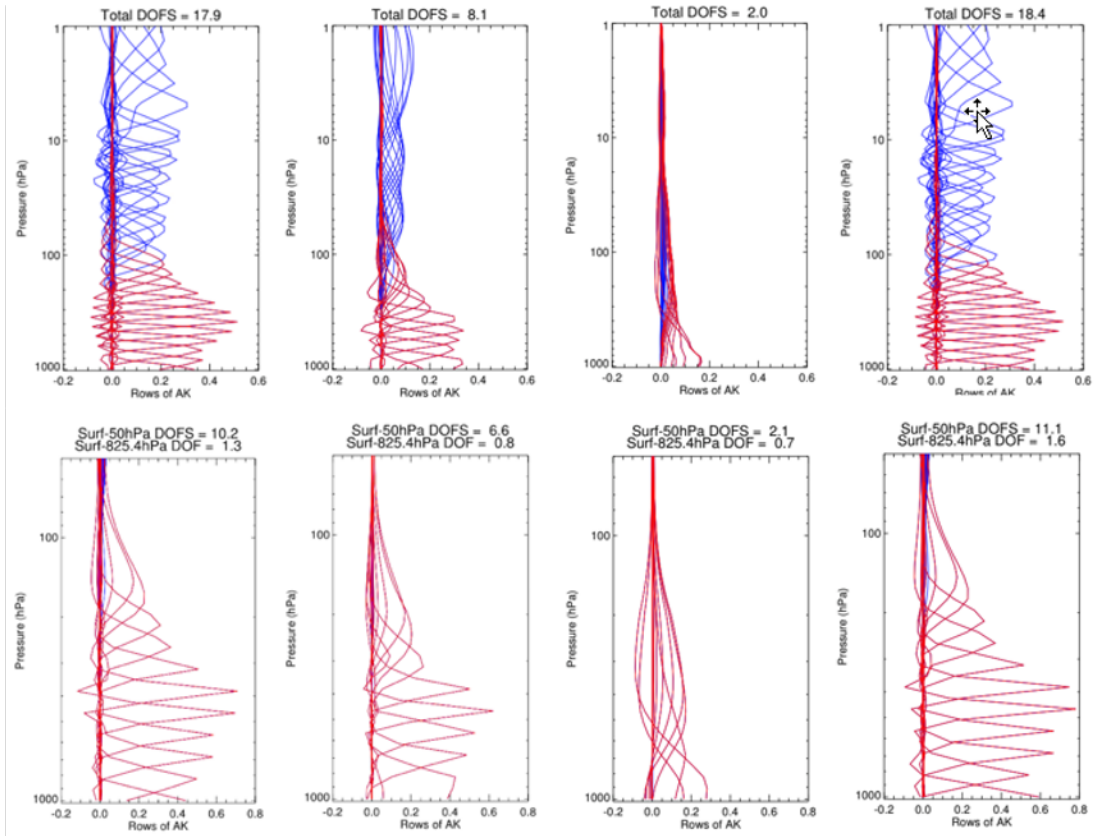
Figure 5: Plots of averaging kernel rows for (top) TATM and (bottom) H₂O. The spectral ranges are (from left to right) VLWIR+LWIR, MWIR, SWIR, and VLWIR+LWIR+MWIR+SWIR. These results are for the Houston case. The blue and red lines refer to averaging kernel rows for pressure levels above and below 100 hPa, respectively.
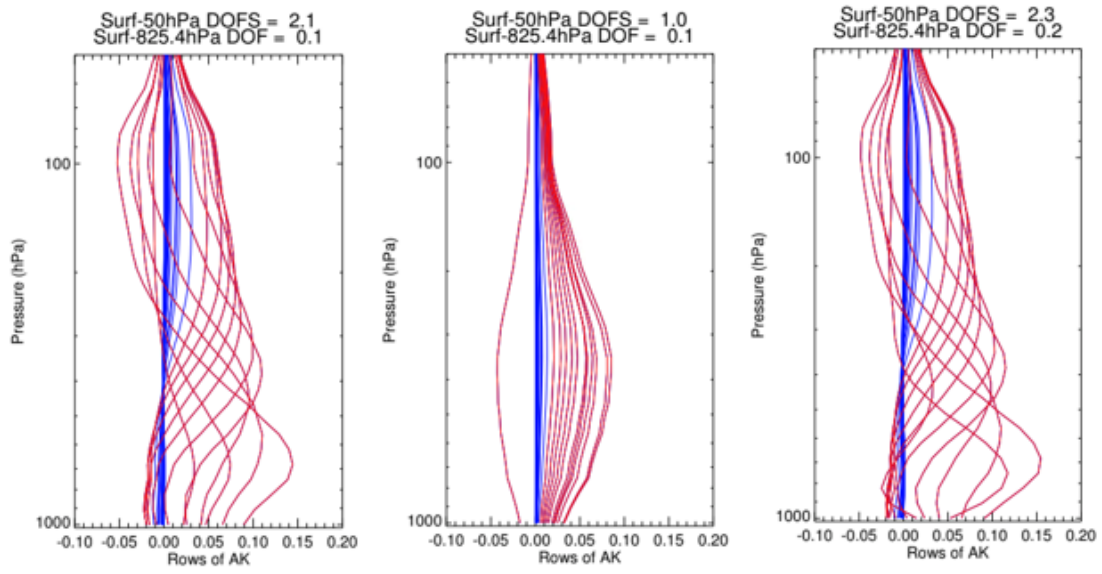
Figure 6: Plots of averaging kernel rows for CO retrievals. The spectral ranges are (from left to right) MWIR, SWIR, and MWIR+SWIR. These results are for the West Virginia case. The color scheme is the same as in Figure 5.
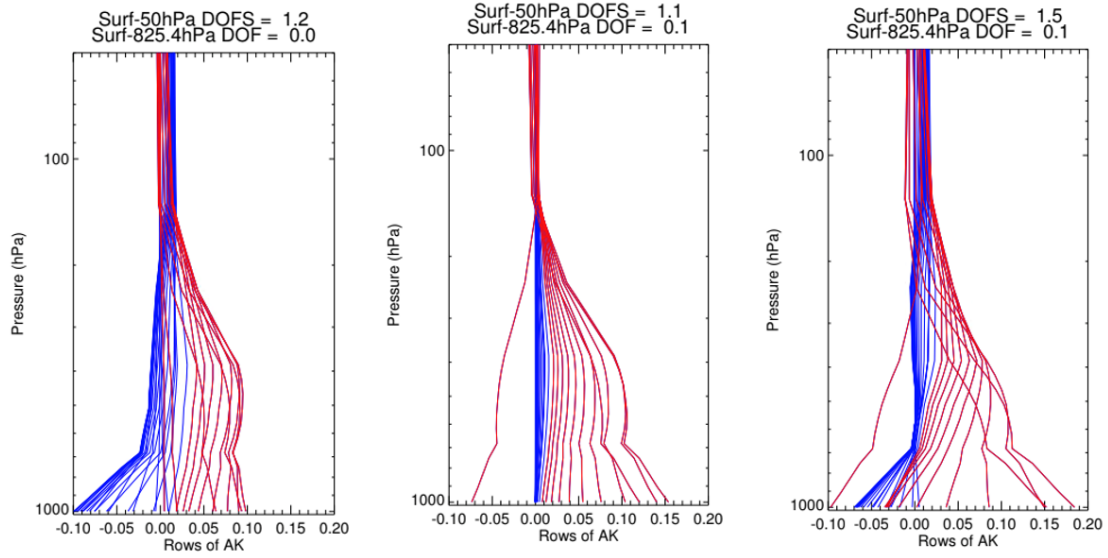
756
757 **Figure 7: Plots of averaging kernel rows for CO$_2$ retrievals. The spectral ranges are (from left to right)**
758 **VLWIR+MWIR, SWIR, and VLWIR+MWIR+SWIR. These results are for the West Virginia case. The color**
759 **scheme is the same as in Figure 5.**
760
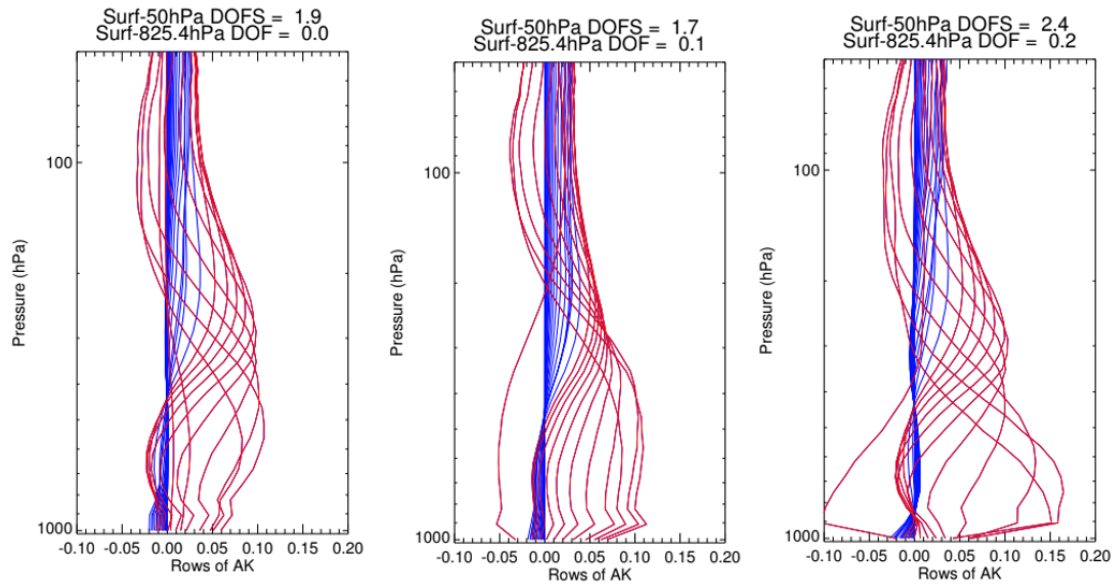
761

762 **Figure 8: Plots of averaging kernel rows for CH$_4$ retrievals. The spectral ranges are (from left to right) LWIR,**

763 **SWIR, and LWIR+SWIR. These results are for the West Virginia case. The color scheme is the same as in**

764 **Figure 5.**

765

766 **Table 1. Spectral ranges and their designations used in this study.**

Designation	Spectral Range (μm)	Spectral Range (cm⁻¹)
VLWIR	>10	<1,000
LWIR	5–10	1,000–2,000
MWIR	3–5	2,000–3,333
SWIR	1–3	3,333–10,000
TIR	>3	<3,333

767

Table 2. Current and planned missions making spaceborne, spectrally resolved measurements of TIR and SWIR radiances. Note that MOPITT was designed to also offer measurements of CH_4, although that did not materialize (hence the gray shading).

Orbit	Instrument/mission	T profile	H_2O		CO		CH_4		CO_2		Winds
		TIR	TIR	SWIR	TIR	SWIR	TIR	SWIR	TIR	SWIR	
LEO	Hyperspectral TIR sounders (AIRS, CrIS, IASI, IASI-NG)	Y	Y		Y		Y		Y		
	MOPITT				Y	Y	(gray)	(gray)			
	GOSAT, GOSAT-2	Y	Y	Y	Y		Y	Y	Y	Y	
	OCO-2/OCO-3			Y						Y	
	TROPOMI			Y		Y		Y			
	TANSAT			Y						Y	
GEO	IRS	Y	Y		Y		Y		Y		Y
	GIIRS	Y	Y		Y		Y		Y		Y
	GeoCarb			Y		Y		Y		Y	Y
	JPL GEO-IR Sounder	Y	Y	Y	Y	Y	Y	Y	Y	Y	Y

771

772

Table 3. Spectral ranges used in this study for simulated retrievals of CO, CH₄ and CO₂.

Molecule	Spectral Ranges (cm^{-1})	Relevant For
Carbon monoxide (CO)	2000–2250 4210–4350	Air quality and carbon cycle (combustion and fire emissions)
Methane (CH$_4$)	1210–1380 4210–4350 6000–6150	Greenhouse gas monitoring and carbon cycle (wetlands, oil and gas, agriculture)
Carbon dioxide (CO$_2$)	650–1100 2250–2450 4810–4900 6170–6290	Greenhouse gas monitoring and carbon cycle (human emissions, status of land and ocean carbon sinks)

773

774 **Table 4. Comparison of JPL GEO-IR Sounder with other state-of-the-art instruments.**

Instrument	GIIRS	IRS	CrIS	JPL GEO-IR Sounder
Status	In space	2023 launch	In space	This study
Nationality	China	EU	US	US
Orbit	GEO	GEO	Polar	GEO
Longitude (°)	104.7 E	0–45 E	N/A	75–137 W
Spacecraft	Dedicated	Dedicated	Dedicated	Hosted payload
GSD, nadir (km)	16 (prototype) 12 (follow-ons)	4	14	4.2 (binned) 2.1 (native)
Spectral range (cm^{-1} unless otherwise indicated)	700–1130 1650–2250 0.55–0.75 μm	680–1210 1600–2250	650 – 1095 1210 – 1750 2155 – 2550	650–10,000*
Resolution (cm^{-1})	0.625	0.625	0.625	NSR** = 0.625, FSR = 0.1
Full Disk Revisit Time (hr)	2–3	1	12	1–2

775 *FTS instrument capability*
776 *** NSR = Nominal Spectral Resolution. FSR = Full Spectral Resolution. FSR mode decreases retrieval biases*
777 *caused by interfering absorbers*

778

35

779 **Table 5. DOFS for TATM retrievals for three spectral (MOPD) and two spatial (GSD) resolution scenarios.**

780 **The values shown here are for the Houston profile.**

Frequency Domain	DOFS (MOPD = 5 cm)		DOFS (MOPD = 2 cm)		DOFS (MOPD = 0.8 cm)	
	2.1 km GSD	4.2 km GSD	2.1 km GSD	4.2 km GSD	2.1 km GSD	4.2 km GSD
VLWIR+LWIR	13.6	17.6	14.2	17.9	14.3	17.9
MWIR	5.1	7.9	5.8	8.3	6	8.1
VLWIR+LWIR+ MWIR	13.8	17.8	14.4	18.1	14.5	18.1
SWIR	0.2	1.6*	0.3	1.8*	0.4	2.0*
VLWIR+LWIR+ MWIR+SWIR	13.8	17.9*	14.6	18.3*	14.7	18.4*

781 * Instrument noise is reduced by a factor of 5 through footprint averaging for the SWIR only,

782 providing an effective GSD of 21 km.

783

784 **Table 6: Same as Table 5 but for H₂O**

Frequency Domain	DOFS (MOPD = 5 cm)		DOFS (MOPD = 2 cm)		DOFS (MOPD = 0.8 cm)	
	2.1 km GSD	4.2 km GSD	2.1 km GSD	4.2 km GSD	2.1 km GSD	4.2 km GSD
VLWIR+LWIR+	7.9	11.2	8.2	11.3	8.2	11.2
MWIR	4.6	6.9	5.0	7.3	4.6	6.6
VLWIR+LWIR+ MWIR	8.3	11.8	8.8	12.1	8.6	11.9
SWIR	1.2	2.2*	1.3	2.1*	1.4	2.1*
VLWIR+LWIR+ MWIR+SWIR	8.3	12.1*	8.9	12.3*	8.7	12.1*

785 * Instrument noise is reduced by a factor of 5 through footprint averaging for the SWIR only,

786 providing an effective GSD of 21 km.

787

788 **Table 7. Trace gas retrieval configurations and DOFS for the West Virginia profile. TATM and H_2O are**

789 **simultaneously retrieved when listed.**

Retrieved Species	Frequency Domain	DOFS (MOPD = 2 cm)		DOFS (MOPD = 0.8 cm)	
		2.1 km GSD	4.2 km GSD	2.1 km GSD	4.2 km GSD
O_3 (TATM, H_2O)	LWIR	3.5	4.0	3.4	4.0
CO	MWIR	1.7	2.1	1.6	2.1
	SWIR	0.08	0.96*	0.1	0.96*
	MWIR+SWIR	1.7	2.3*	1.7	2.3*
CH_4 (TATM, H_2O)	LWIR	1.5	2.0	1.6	2.1
	SWIR	0.7	1.9*	0.8	1.9*
	LWIR+SWIR	1.6	2.7*	1.8	2.8*
CO_2 (TATM, H_2O)	VLWIR	1.0	1.5	1.1	1.6
	VLWIR+MWIR	1.0	1.5	1.2	1.6
	SWIR	0.3	1.1*	0.4	1.1*
	VLWIR+MWIR +SWIR	1.0	1.7*	1.2	1.9*

790 * Instrument noise is reduced by a factor of 5 through footprint averaging for the SWIR only,

791 providing an effective GSD of 21 km.

792

793 **Table 8. Estimates of total and precision errors for JPL GEO-IR Sounder, CrIS and AIRS TATM and H_2O**

794 **retrievals in the troposphere. Note that data used for CrIS and AIRS retrievals were obtained near Houston,**

795 **Texas in August 2020. Averaged retrieved cloud optical depths are limited to less than 0.1, consistent with**

796 **mostly clear-sky conditions.**

	TATM		H_2O (lower-mid troposphere)	
	Total Error	Precision	Total Error	Precision
JPL GEO-IR Sounder (MWIR-only)	0.5–1.5 K	0.2–0.6 K	~8%	~5%
JPL GEO-IR Sounder (Entire spectral range)	0.3–1 K	0.1–0.3 K	~5%	~3%
CrIS	0.5–1.5 K	0.2–0.3 K	10–13%	2–3%
AIRS	0.5–1.2 K	~0.3 K	15–30%	2–5%

797